

Microwave Imaging Using Normal Electric-Field Components Inside Metallic Resonant Chambers

Mohammad Asefi, *Graduate Student Member, IEEE*, Amer Zakaria, *Member, IEEE*,
and Joe LoVetri, *Senior Member, IEEE*

Abstract—A novel 3-D microwave imaging approach performed within a resonant air-filled metallic chamber is introduced and investigated. The new method utilizes the measurements of normal electric-field components at discrete points along the metallic chamber’s wall—near the chamber-wall boundary, the normal-field components are dominant, while the tangential components vanish. The inversion algorithm fully incorporates the resonant features of the low-loss chamber. A numerical study is used to quantify the imaging performance of using this technique compared with the traditional unbounded domain imaging. An experimental system is presented where the electric field is collected using 24 antennas distributed in three circumferential layers around an object of interest located inside the circular-cylindrical metallic chamber. For collecting the normal component of the field, two types of linearly polarized antennas are investigated: $\lambda/4$ monopole antennas and specially designed reconfigurable antennas (RAs), both projecting perpendicularly out from the chamber walls into the enclosure. The measured data are calibrated and then inverted using a multiplicatively regularized finite-element contrast source inversion algorithm. Using 3-D reconstructions of simple dielectric targets, it is shown that utilizing the RAs improves imaging performance due to a reduction in the modeling error introduced in the inversion algorithm.

Index Terms—3-D imaging, contrast source inversion (CSI), finite-element method (FEM), imaging in perfect electrically conducting (PEC), inverse scattering problems, microwave imaging (MWI), modeling error reduction, reconfigurable antenna.

I. INTRODUCTION

MICROWAVE imaging (MWI), which *quantitatively* reconstructs the complex dielectric profile of an object of interest (OI), has been used for a diverse number of applications, and many different inversion algorithms have been developed [1]–[6]. An aspect of MWI systems, which is crucial for obtaining accurate reconstructions, especially systems for biomedical applications such as breast cancer imaging, is the design of the imaging chamber. The chamber not only allows the use of an immersion fluid, but also facilitates the mounting apparatus for the antennas/sensors surrounding the OI. The chamber wall is constructed of either

Manuscript received February 19, 2016; revised June 19, 2016, September 1, 2016, October 3, 2016, and November 1, 2016; accepted November 1, 2016. This work was supported by the Natural Sciences and Engineering Research Council of Canada.

M. Asefi and J. LoVetri are with the Department of Electrical and Computer Engineering, University of Manitoba, Winnipeg, MB R3T 5V6 Canada (e-mail: joe.lovetri@umanitoba.ca).

A. Zakaria is with the Department of Electrical Engineering, American University of Sharjah, Sharjah, United Arab Emirates.

Color versions of one or more of the figures in this paper are available online at <http://ieeexplore.ieee.org>.

Digital Object Identifier 10.1109/TMTT.2016.2627554

dielectric material such as Plexiglas [7], [8] or of conducting metal such as steel or aluminum [9], [10]. For biomedical applications, an immersion fluid with high dielectric constant is used as a matching medium to ensure a maximal amount of energy penetration into the OI [7], [9], [11]. The energy that penetrates the OI is the sole means of interrogating its interior and although having a significant amount of energy flow through the OI does not guarantee that good imaging results will be obtained, it is a necessary requirement.

Loss is typically introduced into the matching medium to reduce the energy arriving at the sensors due to reflections from the chamber walls as well as from any of the antenna apparatus and instrumentation being used that are not included in the inversion model. In this way, if reflections from the chamber walls never make it back to the measurement point, a homogeneous unbounded inversion model can be used allowing efficient computational techniques to be incorporated. If an infinite-extent homogeneous inversion model is used without reducing, such reflections significant modeling errors, which cannot be calibrated out of the data, would be incurred resulting in poor reconstructions [9]. The main drawback of intentionally introducing loss into the imaging chamber is the significant attenuation of the important back-scattered OI signal that results, reducing the signal-to-noise ratio (SNR) that can be expected. Thus, the important but conflicting challenges in MWI system design are: 1) providing a sufficient amount of interrogation energy into the OI; 2) getting this signal back to the receiving antennas with sufficient SNR; and 3) keeping the modeling error low without having to create a sophisticated inversion model that requires unmanageable computational resources.

Utilizing metallic chamber walls allows one to better control and model the unwanted reflections, potentially allowing one to incorporate less loss in the matching medium. This may mean that the use of standard efficient computational electromagnetic techniques that depend on an infinite-extent inversion model is lost, but the overall advantages seem to be worth the effort to incorporate slightly less efficient techniques. In recent years, electromagnetic imaging inside chambers with metallic walls has been investigated both theoretically and experimentally [12]–[15]. Some advantages in using these chambers include: 1) more accurate system modeling in comparison with configurations with dielectric walls (i.e., well-defined perfect electrically conducting (PEC) boundaries that can be modeled precisely versus infinite-extent boundaries, which only approximate the physical system); 2) the ability to use a lossless or low-loss matching medium, which means that

more energy is delivered to the target resulting in higher SNR; 3) less ambiguity about the measured field component near metallic walls, because it is known that the tangential electric field vanishes; and 4) shielding the imaging chamber from the external instrumentation and cabling as well as from any external electromagnetic noise.

Furthermore, for many industrial imaging applications, conductive walls may already be part of the scenario within which an MWI system must be installed; therefore, investigating novel MWI techniques within these conductive walls can be significant for future applications. For example, prototype MWI systems to monitor the quality of stored grain in silos have already been investigated [16]. In addition, varying the shape of the metallic walls becomes a viable technique to introduce various diverse incident fields without modifying the transmitting antenna [15].

In this paper, the novel approach presented in [17] for 3-D MWI inside resonant metallic chambers, where only the normal electric-field components at various locations along the chamber wall are utilized as data, is explored. This technique is complementary to the recent tangential magnetic field technique published in [18]. Although this approach appears “straightforward”, little is known about many of the design parameters, which contribute to successful imaging. Specifically, it is well known that in systems that can be modeled using an infinite-extent background, image quality is related to the number of field sample points [19], and some research has gone into investigating similar criteria for resonant chambers, but in high quality-factor resonant chambers, i.e., those with little loss, the location of the sample points will also be a factor [20]. In Section II, we describe the inversion algorithm which is used. In Section III, we provide the results of a numerical study, based on synthetic data, that not only confirms the feasibility of this approach but also indicates that improved imaging performance is achieved.

In Section IV, we describe the experimental system, its numerical model, and the location of the sources in the model as well as proper location of sampling points. The data calibration technique employed is also described. In this section, we also describe an experimental system that uses thin-wire monopole antennas and analyze the incident field within the chamber for with and without the antennas. We show that the thin-wire monopoles considerably perturb the field distribution within the resonant chamber and therefore must be accurately modeled when incorporated within the inversion model. We also show that poor images result when the inversion model excludes the antennas. Incorporating the coresident monopoles into the inversion model requires large computational resources, which could be eliminated if a means of turning the unused monopoles “OFF” were available. The inversion model could then consist of the simple resonant chamber alone, considerably reducing the computational burden. We also introduce and investigate novel printed “RAs” that can be turned “ON” and “OFF” to achieve this goal. When built using printed-circuit-board (PCB) technology, they can be manufactured consistently, accurately, and inexpensively. In MWI applications, similar “probe” antennas have been used when implementing the differential scattering technique [8],

but here they are introduced within a conventional MWI system.

Conclusions to this paper are presented in Section V.

II. INVERSION ALGORITHM

In general, the mathematical problem associated with MWI is nonlinear and ill-posed. This requires specialized optimization algorithms along with regularization techniques to solve the problem and provide estimates of the relative complex electrical properties of the OI. A review of inversion algorithms is available in [21]. In this paper, the multiplicatively regularized contrast source inversion (MR-CSI) method [22] formulated using the finite-element method (FEM) is used. The details of this implementation can be found in [5] and [23], but for fixing terminology, we briefly describe the inversion algorithm. Note that the results obtained in this paper are applicable to all general-purpose inversion algorithms.

The MR-FEM-CSI method updates two variables in an interlaced fashion until the algorithm’s stopping criteria are met. The two variables are the contrast $\chi(\vec{r})$ and the contrast source $w(\vec{r})$, both the function of position vector \vec{r} and confined within imaging domain \mathcal{D} . The contrast variable within the imaging domain is defined as

$$\chi(\vec{r}) = (\epsilon_r(\vec{r}) - \epsilon_b(\vec{r})) / \epsilon_b(\vec{r}) \quad (1)$$

where $\epsilon_r(\vec{r})$ is the complex relative permittivity to be determined (representing that of the OI) and $\epsilon_b(\vec{r})$ is the numerical background with respect to which the contrast is defined. When no prior information is available, $\epsilon_b(\vec{r}) = \epsilon_b$, the known complex relative permittivity of the homogeneous background medium in the imaging chamber. When prior information about the target is known, a numerical background $\epsilon_b(\vec{r})$ can be used, which incorporates the prior information. Outside the imaging domain \mathcal{D} , $\chi = 0$.

As for the contrast source variables, they are calculated as

$$\vec{w}(\vec{r}) = \chi(\vec{r}) \vec{E}^{\text{tot}}(\vec{r}) \quad (2)$$

where $\vec{E}^{\text{tot}}(\vec{r})$ is the total electric field vector at location \vec{r} inside the imaging domain \mathcal{D} .

The inversion algorithm requires two inputs: the set of scattered fields at the Rx locations, and the simulated incident fields calculated using the numerical inversion model that is adopted for the system. Experimental scattered-field data must be calibrated to the inversion model before being given to the inversion algorithm. The algorithm then iteratively updates $\chi(\vec{r})$ and $\vec{w}(\vec{r})$ within the imaging domain (\mathcal{D}) until a best match is obtained between the numerically calculated scattered field, $E_{\text{simulated}}^{\text{sct}}$, and the calibrated measured (or the numerically generated) scattered field, $E_{\text{measured}}^{\text{sct}}$. In addition to this data-error functional, a domain-error function is formulated and combined to form a single CSI functional

$$\mathcal{F}^{\text{CSI}}[\vec{w}_t, \chi] = \eta_S^E \sum_{t=1}^{N_t} \|\vec{\rho}_t^E\|_S^2 + \eta_D^E \sum_{t=1}^{N_t} \|\vec{\rho}_t^E\|_D^2. \quad (3)$$

Here, the data-error vector is defined as $\vec{\rho}_t(\vec{x}) \triangleq \vec{E}_t^{\text{sct,data}}(\vec{x}) - \mathcal{L}_S \vec{w}_t(\vec{x}')$, and the domain-error vector as $\vec{\rho}_t(\vec{x}) \triangleq \chi(\vec{x})(\vec{E}_t^{\text{inc}}(\vec{x}) + \mathcal{L}_D \vec{w}_t) - \vec{w}_t(\vec{x})$. Details on the normalization

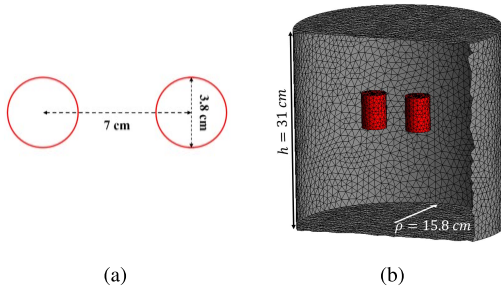


Fig. 1. Illustration of (a) top view of the targets and (b) their spatial location within the imaging chamber.

factors that balance these two functionals, η_S^E and η_D^E , can be found in [5].

III. NORMAL COMPONENT NUMERICAL IMAGING STUDY

The effectiveness of inverting the normal component of the electric field on a PEC chamber's wall can be studied numerically using synthetically generated data. This is done by first evaluating the performance of an unbounded imaging system, capable of exciting and collecting all three components of the electric field (E_ρ , E_ϕ , and E_z), as a function of frequency, for different sets of sources and Rxs placed around some fixed targets. The boundaries of this problem are then replaced with PEC boundaries and the imaging performance is analyzed as a function of the amount of data, frequency of operation, the type of the imaging chamber, and configuration of the transceivers. For these studies, two cylinders with a diameter of 3.8 cm, a height of 5.3 cm, and a relative permittivity of 3 are used as the targets within the imaging chamber, as shown in Fig. 1. The dimensions of the problem domain are also shown in Fig. 1. The numerically generated data are directly used as input to a FEM-CSL algorithm for the reconstruction of the dielectric profile of the targets. As the point of this paper is solely to evaluate the performance of the imaging system when normal component data at the PEC boundaries are used, no noise is added to the numerical data and a single mesh is used for both generation of the forward data and the inversions. Thus, an intentional “inverse crime” is incurred.

As the first case, multiple sets of numerical data were generated for a free-space problem. For this case, numerical data sets were generated and inverted at multiple individual frequencies when all three polarizations of the electric field were excited and collected at four, six, seven, nine, and eleven positions within the imaging chamber. These positions were selected to be 3.2 cm away from numerical boundary of the problem where absorbing boundary conditions (ABCs) were applied. The total number of tetrahedra in the complete mesh is 152 877, while the number of tetrahedra inside the imaging domain is 51 885. Note that the imaging domain is restricted to consist of only the spatial region within a cube surrounding the targets.

The inversion results, at 1.7189 GHz, for this free-space case when 18 and 27 transmitter/receiver (Tx/Rx) positions/polarizations are used are shown in Fig. 2. It can be

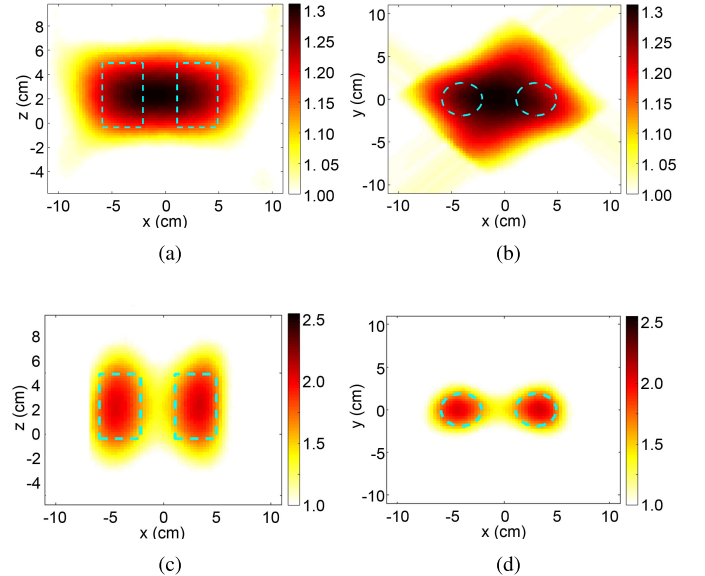


Fig. 2. 2-D cross-sectional plots of the reconstructed dielectric permittivity of the targets at 1.7189 GHz for cases that numerical data are generated and inverted when (a), (b) six and (c), (d) nine Tx/Rx positions (each including three polarizations) are utilized in an unbounded problem (free space). Dashed lines: true position of the targets.

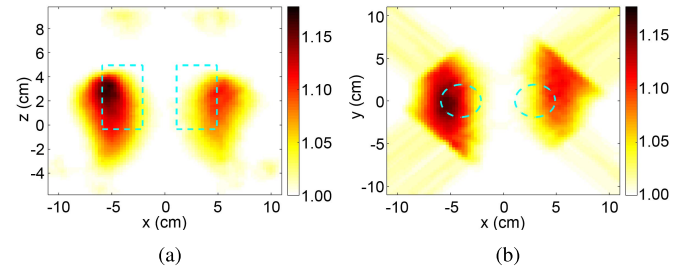


Fig. 3. 2-D cross-sectional plots of the reconstructed dielectric permittivity of the targets at 1.7189 GHz when numerical data are generated and inverted for six Tx/Rx positions (each including three polarizations) in a highly resonant chamber. (a) Plane $y = 0$. (b) Plane $z = 2.3$ cm. Dashed lines: true position of the targets.

observed that, as expected, as the number of transceivers (i.e., data points) increases, the inversion result improves.

For the second case, the boundary of the problem is changed to PEC and the numerical data are collected for the same scenarios. The plots of the reconstructed dielectric profile of the targets when 27 Tx/Rx positions are utilized are shown in Fig. 3.

It can be observed that, even though the targets are poorly reconstructed, the inversion results are qualitatively improved compared with the previous case with the same amount of data points. This is because more of the energy within the PEC boundaries, as compared with the ABC case, interrogates the targets. In addition, the existence of cavity modes can help increase the measured field values at the Rx points. Note that, as before, these results can be enhanced by increasing the amount of data.

As mentioned previously, one of the main advantages of metallic chambers, in experimental setups, is that their

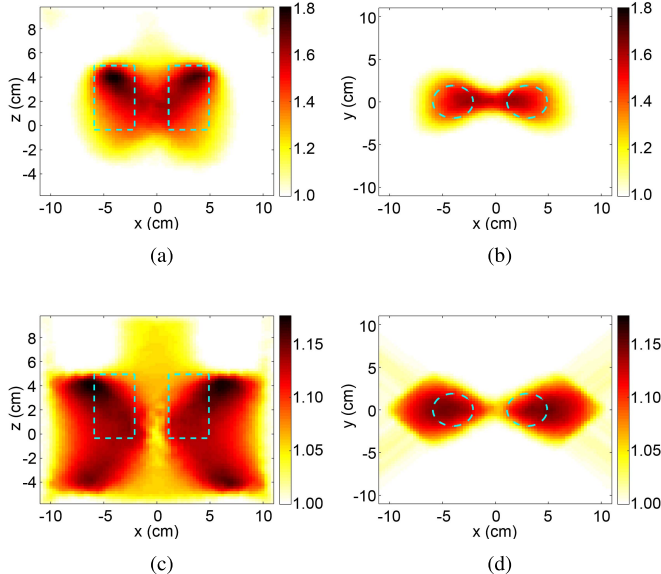


Fig. 4. 2-D cross-sectional plots for the reconstruction of the dielectric permittivity for the two targets when numerical data are generated and inverted for 18 ρ -polarized Tx/Rx pairs in a highly resonant chamber at (a), (b) 1.7189 (close to TE_{213}) GHz and (c), (d) 1.7310 GHz (TM_{021}).

conducting boundary electromagnetically isolates/shields the interior of the chamber from the outside. This shielding results in reduced modeling complexity by eliminating the need to numerically model external objects (such as cables) in the near field of the antennas. If antennas are placed away from the conducting boundary, similar to the second case, their presence can significantly perturb the fields within the chamber and increase modeling requirements. To avoid this and to take advantage of the conducting boundaries, the antennas can be moved to the boundary, but because the tangential components of the electric field vanish close to the conducting boundaries, only the normal component of the electric field needs to be measured. Note that because the imaging problem's boundary is in the form of a cylinder, the normal component of the electric field is ρ -polarized. This scenario is used for the third case where the number of Tx/Rx points is tripled (i.e., 12, 18, 21, 27, and 33 Tx/Rx points) so as to keep the number of data points the same. Similar to the previous cases, numerical data are collected and inverted for different Tx/Rx combinations and frequencies. The inversion results for two frequencies are shown in Fig. 4. It can be seen that even though the targets are not completely discernible at 1.7189 GHz, which is close to the resonance frequency of a TE mode (TE_{213}), the performance of this system is better than the free-space case. In addition, the reconstructed permittivity of the targets in this case is closer to the true value. One reason for the improved reconstructed permittivity is the increased number of spatial sampling points.

The problem with highly resonant chambers is that the results can be highly dependent on the frequency at which the inversion is performed. For example, the inversion results at 1.7310 GHz, which is close to the resonance frequency of the TM_{021} mode, are shown in Fig. 4(c) and (d) and we see that at this frequency, we obtain a poor reconstruction of the targets, both quantitatively and qualitatively. For this

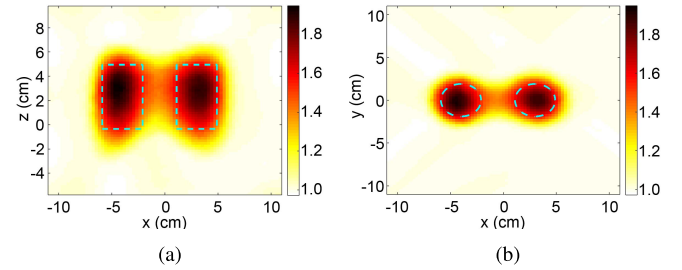


Fig. 5. 2-D cross-sectional plots for the reconstruction of the dielectric permittivity for the two targets at 1.7189 GHz when numerical data are generated and inverted for 18 ρ -polarized Tx/Rx pairs in a chamber with low loss background. (a) Plane $y = 0$. (b) Plane $z = 2.3$ cm. Dashed lines: true position of the targets.

orientation of TxS and RxS, we have observed that the inversion results at frequencies close to, or right at, the resonance frequencies corresponding to the TM modes are very poor compared with those close to, or right at, the resonance frequencies of the TE modes. This inconsistent behavior is not desirable, especially for multifrequency imaging as well as for imaging within irregular chambers where the resonant frequencies, and corresponding field distributions, are difficult to predict.

To resolve this issue, one approach is to dampen the modes in the imaging system by adding a small amount of loss. Such loss can be introduced in two ways, adding loss to the dielectric background medium (not a practical solution in air) or allowing some energy to escape the chamber. Adding loss to the dielectric background makes the imaging performance more predictable. To illustrate this approach, the background permittivity inside the metallic enclosure is changed from a value of 1 to $1 - j0.3$. The reconstructed dielectric profile of the targets at 1.7189 GHz, for 18 ρ -polarized TxS and RxS, is shown in Fig. 5. The inversion results at multiple frequencies show that not only does the imaging performance become more stable as a function of frequency, but also, the error in the inversion results is reduced compared with the case of the lossless background (i.e., a highly resonant chamber).

Adding a lossy background can cause a significant reduction in the SNR, a problem that the second approach of damping the modes does not suffer. Thus, simply removing the top lid of the chamber (i.e., setting the top of the mesh to an ABC) will significantly dampen the modes because of the loss of energy through the top of the chamber. The effect of opening the top of the imaging chamber on the percentage error is illustrated by the reconstructed dielectric profile of the targets at 1.7189 GHz shown in Fig. 6. The inversion results at multiple frequencies show that opening the top improves the imaging performance of the system significantly while maintaining most advantages of a PEC enclosure.

To summarize the performance of these different MWI scenarios, the five study cases are tabulated in Table I and the plots of the percentage error in the permittivity of the reconstructed targets (taken over the whole imaging domain) for the 18 and 27 Tx/Rx pair combinations are shown in Fig. 7.

It can be observed that, as expected, the percentage error is slightly reduced as the frequency increases (increasing the

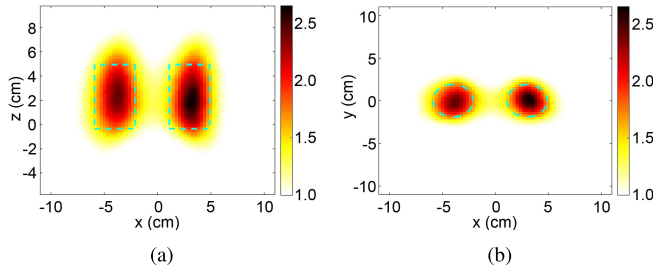


Fig. 6. 2-D cross-sectional plots for the reconstruction of the dielectric permittivity for the two targets at 1.7189 GHz when numerical data are generated and inverted for 18 ρ -polarized Tx/Rx pairs in an open top chamber. (a) Plane $y = 0$. (b) Plane $z = 2.3$ cm. Dashed lines: true position of the targets.

TABLE I
STUDY CASES FOR EVALUATION OF THE PERFORMANCE
OF MWI INSIDE METALLIC ENCLOSURES

Case	Boundary	$\epsilon_b(\vec{r})$	Tx/Rx polarization	Tx/Rx radial position
1	ABC	1	E_ρ, E_ϕ, E_z	$\rho = 12.6$ cm
2	PEC	1	E_ρ, E_ϕ, E_z	$\rho = 12.6$ cm
3	PEC	1	E_ρ	$\rho = 15.7$ cm
4	PEC	$1 - j0.3$	E_ρ	$\rho = 15.7$ cm
5	PEC/ABC	1	E_ρ	$\rho = 15.7$ cm

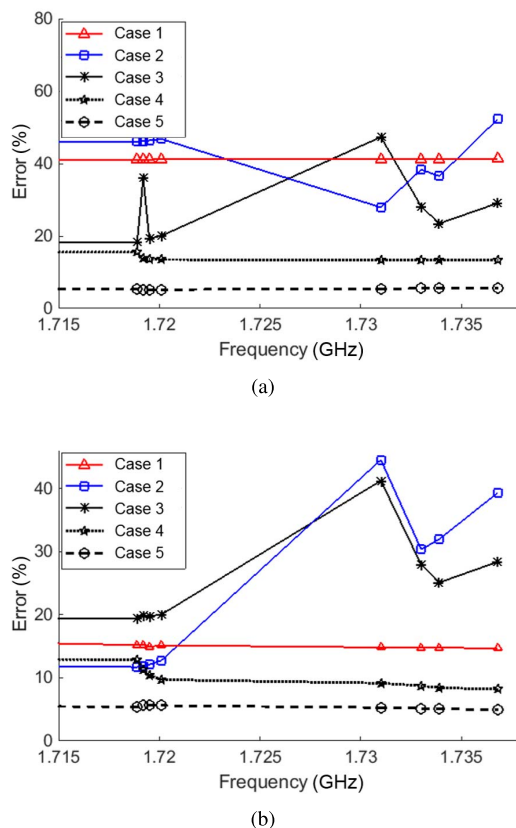


Fig. 7. Plots of the percentage error between the permittivity of the true numerical targets within the imaging domain and that of the reconstruction results for (a) 18 and (b) 27 Tx/Rx pairs, including all polarizations.

frequency generally increases the resolution of imaging methods) for the unbounded problem (case 1). This error reduction is not significant because of the small change in the frequency.

However, for the cases where the boundary is set to PEC (cases 2 and 3), the imaging performance becomes unpredictable. In fact, the error on these plots can be divided into two parts: the first part containing the errors for frequencies below 1.725 GHz (on the graph) and the second part containing the higher frequencies (shown on the graph). The first set of frequencies are either close to, or right at, the resonance frequencies of TE modes, while the second set of frequencies are either close to, or right at, the resonance frequencies of TM modes. As can be observed, the imaging performance is relatively predictable at frequencies close to the resonant frequencies of the TE modes, while it is very inconsistent at frequencies close to the resonant frequencies of the TM modes. This is most likely due to the orientation of the received fields, which are the normal component of the electric fields at the walls of the chamber and the fact that the TE modes contain more energy in this polarization.

This graph also shows that damping the modes significantly improves the performance of this imaging modality. In addition, the performance of this imaging modality in case five, where damping of the modes is obtained through opening the top of the chamber, is better than that of case four, introducing loss, because more energy that has interrogated the targets reaches the Rx points.

IV. NORMAL COMPONENT METALLIC CHAMBER SYSTEM

This section includes a description of the experimental system used for validation of the concept of adopting normal electric-field components inside metallic chambers as data for imaging. One of the greatest challenges in using such chambers is that any antenna that is introduced into the chamber will greatly perturb the field distribution and therefore must be taken into account in the inversion model. Of course, the disadvantage of modeling the antennas is that it increases the computational complexity of the problem and the time required to invert the measured data. Therefore, utilizing antennas that are simple to model is important to reduce the computational burden. The normal electric-field component at several locations along the interior walls of the chamber can be effectively measured using simple wire monopole antennas protruding normally into the interior of the chamber.

A preliminary numerical model for a simple system that includes two $\lambda/4$ wire antennas for the Rx and Tx is first investigated in order to determine if a simple numerical model can be utilized. The perturbation of the fields due to the use of several coresident thin-wire antennas in the experimental system is then investigated and found to create significant modeling error if the wire antennas are not incorporated within the numerical model. Such a numerical model would impose severe numerical costs to the 3-D inversions, and therefore, in the final part of this section, specially designed RAs (i.e., antennas whose effective length can be changed using active circuit elements) are introduced to minimize the modeling error while keeping the numerical model simple.

A. System Configuration

For the experimental system, we consider an air-filled cylindrical chamber having PEC walls with an open top.

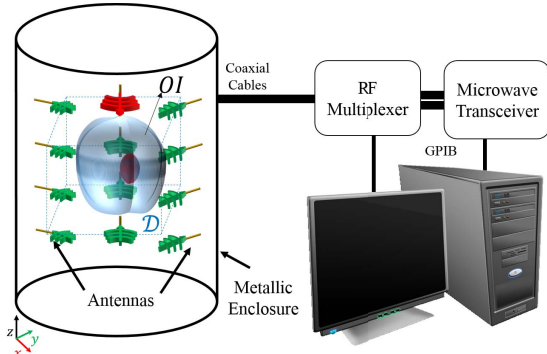


Fig. 8. Block diagram of the MWI system.

The diameter is chosen to be 31.5 cm and its height is 31 cm. An open-ended waveguide of these dimensions will have the fundamental mode of TE_{11} with a cutoff of 556 MHz, while a circular cavity of this dimension will have a fundamental mode of TM_{010} with a cutoff frequency of 726 MHz.

A block diagram of the experimental imaging system is shown in Fig. 8. The initial system consists of a total 24 thin-wire $\lambda/4$ monopoles projecting radially from the cylindrical surface of the chamber in three circumferential layers, with each layer consisting of eight equally distributed antennas (we simply utilize the center conductor of the coaxial cable feeding the antenna). Thus, each antenna is sensitive to the ρ -polarized electric field. That is, it excites or collects (depending on whether it is acting as a Tx or Rx) the normal component of the electric field at the chamber's wall. Each antenna is connected to one of the ports of a 2×24 matrix switch (Agilent 80705A-K24). The switch enables each antenna to act as either a radiator, delivering energy into the chamber, or a Rx, collecting the electric field energy. The switch is followed by a vector network analyzer (VNA) that is used as the system's transceiver; it delivers microwave signals to the antennas via the matrix switch, and measures the signals received by the antennas. The measured data are then calibrated and used as input to our FEM-CSI inversion algorithm, which reconstructs a 3-D dielectric map within the imaging domain (D) shown in Fig. 8. Note that the imaging domain may extend to the walls of the chamber.

B. Numerical Inversion Model

The simplified numerical model adopted for the measurement system is an open-top cylindrical PEC enclosure without antennas so as to reduce the computational cost of the problem. The sources are modeled as Hertzian dipoles and the normal electric field is collected at various distances from the chamber wall. The choice of how far to place these source and Rx locations from the walls of the chamber was made by comparing the accuracy of this model with that of the equivalent experimental system containing only two thin-wire monopoles. One monopole is used as the Tx and the other is used as the Rx.

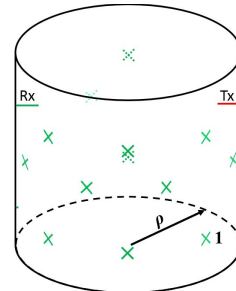


Fig. 9. Tx position and 16 measurement point locations inside the imaging chamber. The measurement locations are marked with X. The number one marks the position of the first Rx point and the rest of the positions are numbered in a clockwise order from the bottom to the top.

Two types of tests were performed to evaluate these distances. The measurement chamber was modeled in an electromagnetic simulation software (FEKO) with the transmitting antenna modeled as a 3.1-cm thin wire and excited using a voltage source at its base next to the chamber wall for both types of tests. A frequency range of 0.5–1.8 GHz was chosen, but the thin-wire length was kept the same through these tests (corresponding to $\lambda/20$ and $\lambda/5$). For these tests, the Tx was fixed at a certain location, while Rx measurements were made at multiple locations inside the imaging chamber. The test points, Rx or Tx, are shown in Fig. 9. Note, FEKO was used for this part of the study because of its accurate thin-wire model, not available in the FEM code used for the inversion model.

The first type of test was conducted to determine the optimal distance from the chamber wall at which to output the electric field in the numerical model so as to best approximate what is collected by the receiving monopole. Thus, for a fixed Tx location, the ρ -polarized electric field was output at three different distances from the chamber wall in the FEKO model. The plot of Fig. 10(a) shows a comparison between the simulated fields and the measured fields at all 16 Rx locations at 1.2 GHz. Note that the measurement data are collected as S-parameters using a VNA. These S-parameters are converted into electric fields at the Rx point location using the methodology provided in [24]. The percentage error (calculated for the ℓ^2 norm) between the measured and the simulated field at different distances from the chamber wall for different frequencies is shown in Fig. 10(b). It can be seen that choosing a Rx location, in the model, right at the chamber wall, $\rho = 15.8$ cm, does not simulate the dipole antenna well, whereas choosing it a slight distance away from the wall provides less error (2–4 mm from the wall).

With this knowledge of the optimum position of the Rx points, the second type of test was conducted to determine the optimal distance from the chamber wall at which to place a simple Hertzian dipole to excite the electric field in the numerical model so as to best approximate the electric field excited by the transmitting monopole (this becomes the simplified “position of the transmitters” in the FEM inversion model). In this test, the reference was set to be the FEKO-simulated field due to its fixed thin-wire monopole, measured at a radius of $\rho = 15.3$ cm corresponding to

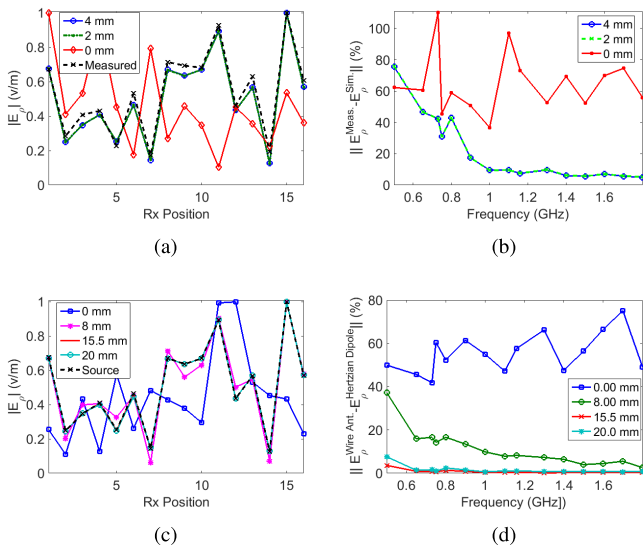


Fig. 10. Plots of (a) normalized measured electric field and the simulated electric field for Hertzian dipoles at different distances from chamber wall as a function of position at 1.2 GHz, (b) error between the different simulated cases and the measurement as a function of frequency for this case, (c) normalized simulated electric field for a quarter-wave radially positioned monopole antenna and the simulated electric field for Hertzian dipoles at different distances from chamber wall as a function of position at 1.2 GHz, and (d) error between the different Hertzian models versus the thin-wire monopole model as a function of frequency for this case.

a distance of 0.5 cm from the chamber wall (a good performing distance obtained from the previous test). The thin-wire monopole in the FEKO model was then replaced by a Hertzian dipole at different distances from the chamber wall and the resulting received fields were output at each of the 16 measurement locations for four different Hertzian dipole distances and compared with the reference case. The results of this test are shown in Fig. 10(c) and (d). These results again show that the Hertzian dipole should be placed a slight distance away from the chamber wall to minimize the modeling error. A distance approximately corresponding to the midpoint of the wire, 1.55 cm away from the wall, was chosen as a good modeling point for the Tx location.

C. Measurement Data Calibration

In addition to a numerical inversion model, the scattered electric field must be calibrated. Measurements provide the S_{12} values between the Tx and Rx ports. These have to be converted into calibrated field values for the model. Several calibration techniques are available [8], [25]–[27]. In this paper, the calibration is based on the incident-field values for the empty chamber. Thus, two measurements are collected inside the imaging chamber: 1) incident-field measurements of the empty chamber (U^{inc}) and 2) total field measurements with the presence of the OI (U^{tot}). The calibrated scattered field is given as

$$E_{r,t}^{sct, cal} = \frac{E_{r,t}^{inc}}{U_{r,t}^{inc}} (U_{r,t}^{tot} - U_{r,t}^{inc}) \quad (4)$$

where t and r denote the active Tx and Rx, and the simulated incident-field is denoted as $E_{r,t}^{inc}$.

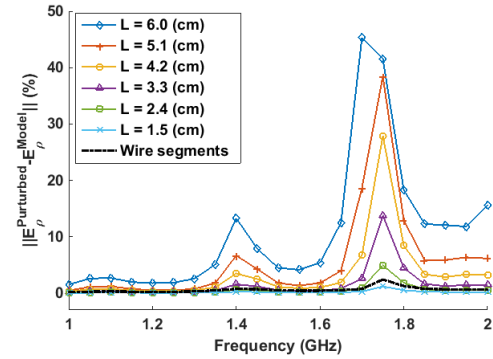


Fig. 11. Plot of the difference between the ρ -component of the electric field inside the imaging chamber due to introducing wire antennas of different sizes as well as segmented wire pieces in comparison with the simplistic, unperturbed chamber. L denotes the antenna length.

After calibration is complete for each Tx/Rx pair, the calibrated data are used as input for the inversion algorithm.

D. Inversion of Data Taken With Thin-Wire Monopoles

The initial measurement system includes 24 thin-wire coresident monopole antennas as Txs and Rxs inside the previously described open-top chamber. These coresident antennas will perturb the field creating a large mismatch between the simplified model, which does not include the coresident antennas and the actual experimental system. This is especially true when higher order modes exist in the chamber (note that the first waveguide mode inside the air-filled imaging chamber is the TE₁₁ mode which starts at 556 MHz). The effect of the coresident antennas on the field distribution within the chamber, as a function frequency, is shown in Fig. 11. In this graph, the ℓ^2 norm of the difference between the FEKO-simulated electric field at different locations inside the simplistic model described in Section IV-B and five other chambers with coresident thin-wire monopoles of different lengths are shown. It can be observed that, as the length of the passive coresident wire antennas is reduced, so is the total mismatch between the two models. At some frequencies, because of the location of the antennas with respect to the mode pattern, the error remains high between the simplistic model and the model incorporating all the coresident antennas. In general, minimally perturbing frequencies are lower frequencies where the lengths of the coresident antennas as well as the number of modes are small. The low frequencies, however, imply large wavelengths and consequently low resolution.

As a first attempt, it was decided to invert data taken at 1.47 GHz for the two nylon cylinders shown in Fig. 12 having a diameter of 3.8 cm and a height of 5.3 cm. Thin wires having a length of 5.1 cm, corresponding to monopole antennas with a resonance frequency of 1.47 GHz in free space, were utilized. The relative permittivity of these nylon cylinders is $\epsilon_r = 3.2$. The two nylon cylinders were hung inside the imaging chamber with the spacing between their axes being 8 cm. The reconstruction results using FEM-CSI are shown in Fig. 13. Dashed lines illustrate the actual location of the cylinders inside the imaging domain. It can be observed that at this frequency, due to the small

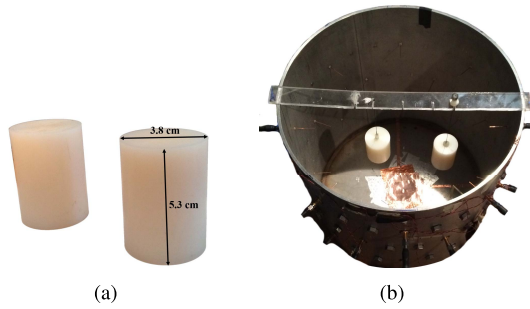


Fig. 12. Picture of (a) nylon cylinders used as targets and (b) imaging chamber.

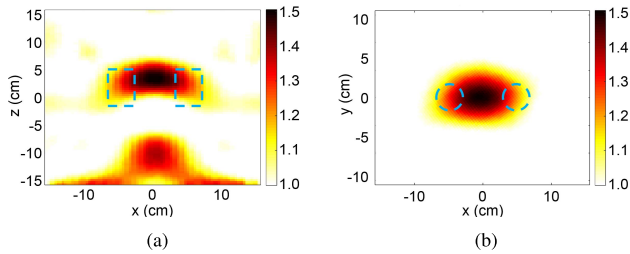


Fig. 13. Two nylon cylinders reconstructions at 1.47 GHz using $\lambda/4$ monopole wire antennas. The 2-D cross-sectional plots at planes (a) $y = 0$ cm and (b) $z = 2.4$ cm.

size of the objects ($\lambda/5 \times \lambda/3.5$), as well as the small spacing between the two objects ($\lambda/4$) and the modeling error, the reconstructed images are poor. Not only are the objects not resolved but artifacts appear in the images. To quantify the error for the experimental results, the true position, geometry, and permittivity of the targets were estimated and used to calculate the percentage error between the reconstructed dielectric map and its true value within the imaging domain. The percentage error for this case was found to be 33.25%.

In an attempt to better resolve the cylinders, the imaging frequency was increased from 1.75 to 1.90 GHz while maintaining the same size of the antennas. The inversion results for these cases are shown in Fig. 14. At higher frequencies, the number of coexisting modes inside the chamber increase (from <6 modes at frequencies below 1.5 GHz to greater than ten modes at frequencies over 1.67 GHz). The main disadvantage with this increase in the number of modes is the need for finer spatial sampling (i.e., an increase in the number of transmitting and Rx antennas). It can be observed that, at 1.75 GHz, a frequency for which there is significant modeling error as can be seen from Fig. 11, the inversion results are quite poor, whereas at 1.90 GHz, even though the modeling error is higher than at 1.47 GHz, the two objects are resolved. However, due to the modeling errors, the reconstructed shape and the permittivity are not accurate and many artifacts show up in the reconstructed image. The percentage errors for these reconstructions are 28.47% and 20.43% for the 1.75 and 1.90 GHz cases, respectively. It should be noted that the use of higher frequencies requires increased number of tetrahedrons inside the imaging domain, which results in an increased number of unknowns and computational cost. Moreover, as the frequency increases, the penetration depth decreases

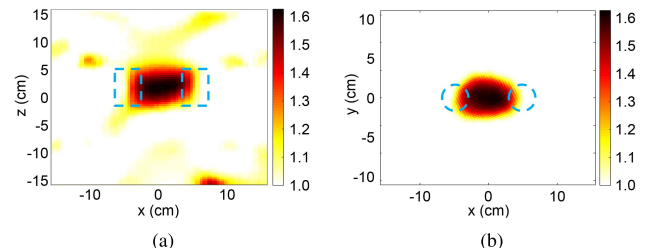


Fig. 14. Reconstruction results for two nylon cylinders using $\lambda/4$ monopole wire antennas: The 2-D cross-sectional plots at planes $y = 0$ cm and $z = 2.4$ cm at (a), (b) 1.75 and (c), (d) 1.90 GHz, respectively. Dashed lines: true position of the targets.

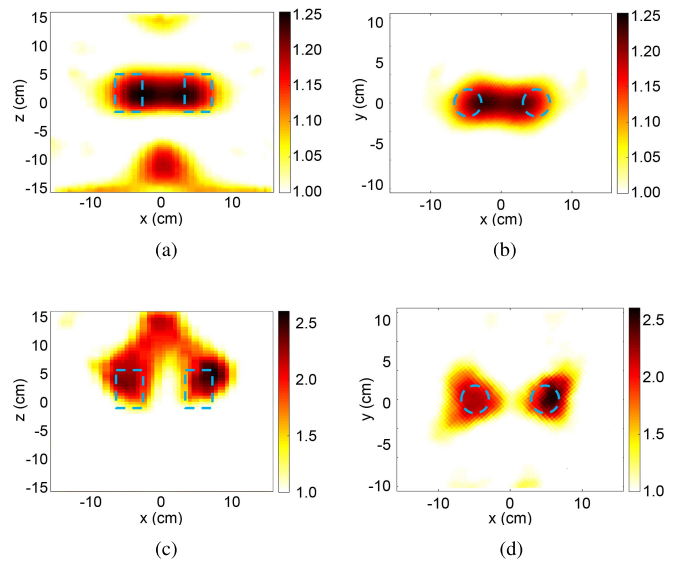


Fig. 15. Reconstruction results for two nylon cylinders using miniaturized $\lambda/12$ monopole wire antennas. The 2-D cross-sectional plots at planes $y = 0$ cm and $z = 2.4$ cm at (a), (b) 1.47 and (c), (d) 1.75 GHz, respectively. Dashed lines: true position of the targets.

which imposes practical limitations for imaging of biological tissues.

As shown in Fig. 11, the modeling error can be reduced in the simplistic model by reducing the length of the antennas. To test this possibility, the $\lambda/4$ monopoles were replaced by $\lambda/12$ monopoles at 1.47 GHz. Data for the same two nylon cylinders were collected and inverted. Fig. 15 shows the inversion results obtained for this case, 1.47 GHz, as well as for 1.75 GHz.

It can be observed that the reconstructed dielectric profile is enhanced significantly (qualitatively) for both frequencies, and especially at 1.75 GHz. The percentage errors for this case

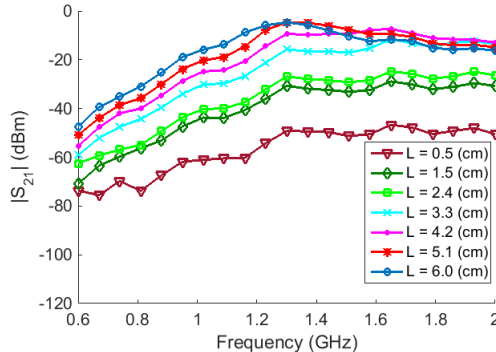


Fig. 16. Effect of antenna size reduction on the received measured electric field. L stands for the antenna length.

are 47.03% and 8.91% for 1.47 and 1.75 GHz, respectively. The reduced error for the 1.75 GHz case is because the smaller antenna size significantly reduces the modeling error. However, such a reduction in antenna size reduces the SNR and it is conjectured that it is this effect that produces the artifacts in the reconstructed images. The reduction in SNR is shown in Fig. 16, where a thin-wire transmitting antenna of length 5.1 cm was placed inside the measurement system and thin-wire antennas of different sizes were used for reception (no other antennas were present). Fig. 16 shows that the received signal is significantly reduced as the length of the receiving antenna is made shorter.

Thus, a solution which maintains the SNR of the received data while minimizing the perturbation of the field by the coresident passive antennas, as compared with the simple numerical model used in the inversion, is required. From the graph of Fig. 11, it is observed that when the wire monopoles are replaced with antennas which are made up of segmented pieces of wire rather than a solid wire (dashed line in Fig. 11), their perturbation effect is minimal. Thus, in order to maintain the high sensitivity of quarter-wavelength Tx/Rx monopoles while minimizing the modeling error, reconfigurable monopoles are adopted.

E. MWI With RAs

The same MWI system was outfitted with printed reconfigurable monopole antennas (RAs). These were fabricated on double layer PCBs, with the current prototype incorporating five p-i-n diodes. Each antenna also includes two capacitors and resistors for dc coupling/decoupling purposes and a pair of twisted wires is utilized for dc biasing. The circuit schematic and a depiction of one of the RAs are shown in Fig. 17. The p-i-n diodes, used to control the operation of the RAs in different modes, are controlled through a driver circuit, which biases or unbiases the antennas. If an antenna is biased, its p-i-n diodes are “ON” or “shorted.” If an antenna is unbiased, its p-i-n diodes are “OFF” or “opened.”

To illustrate the performance of these antennas, two RAs were placed on opposite sides (along the radius of the chamber) inside the imaging chamber. A graph of S_{11} and S_{12} for the biased and unbiased cases of one of the antennas is shown in Fig. 18. This graph shows that when the antenna is

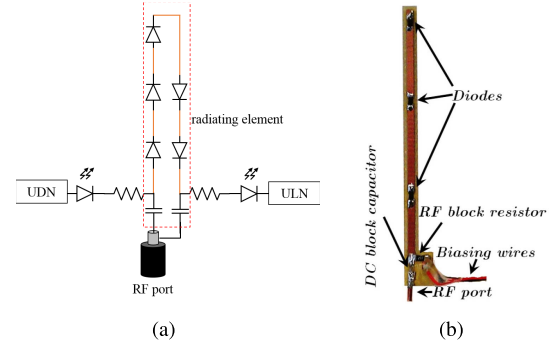


Fig. 17. (a) Circuit diagram of the reconfigurable monopole and (b) photograph of one layer of the fabricated antenna. UDN and UDN are Darlington transistor arrays, which are used to drive the diode and the length of the antenna is 5 cm.

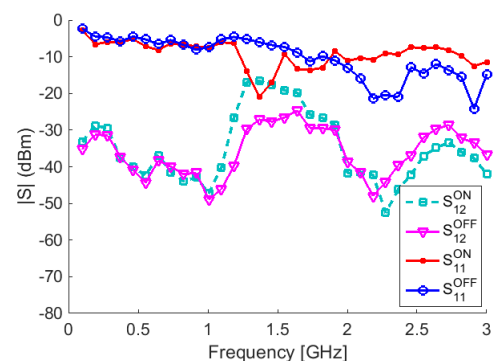


Fig. 18. S-parameters of a RAs in the active (ON) and inactive (OFF) cases.

in the active mode, it acts as a monopole antenna within a certain frequency band with reasonable reflection coefficient. However, when it is deactivated, the reflection coefficient of the antenna becomes relatively flat and close to zero over the same frequency band. Note that S_{21} also drops significantly over a relatively wide bandwidth. Because of the small size (compared with wavelength) of the conductor segments forming the antenna, this ensures that the perturbation of the antenna in the “OFF” mode is minimal over this frequency band.

To collect data using this system, antennas are placed in one of two modes.

- 1) *Transmit or Receive Mode:* The diodes are forward biased (“ON”) effectively shorting the gaps between the printed conducting elements of the antenna.
- 2) *Passive Mode:* The diodes are reversed biased (“OFF”) effectively segmenting the antenna into short pieces of wire.

The data collection is handled as follows. First, the desired Tx and Rx antennas are placed into the proper mode using a dc-driver circuit and the two ports of the VNA, used as our transceiver, are routed to these antennas utilizing an RF-switch. All remaining coresident antennas are placed in the passive mode using the dc-driver circuit. Note, by choosing a proper number and size for the segments making up each antenna, the perturbation effect of the coresident antennas is significantly decreased.

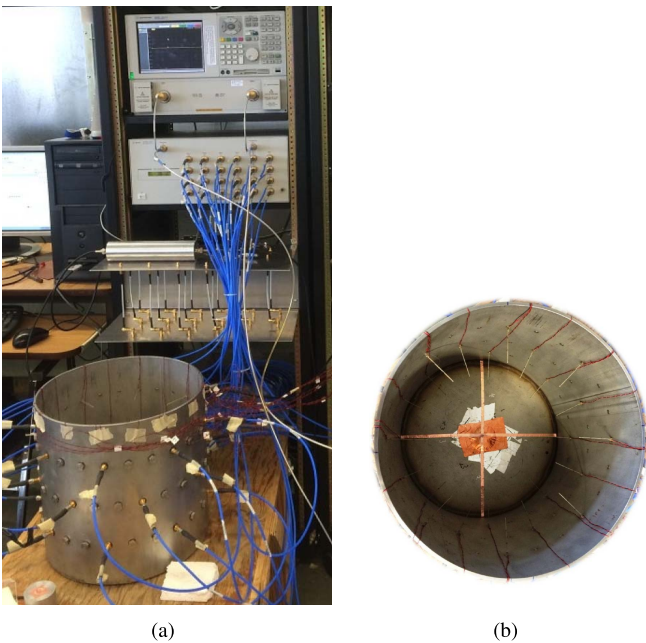


Fig. 19. (a) Photograph of an air-based prototype MWI system and (b) its metallic imaging chamber.

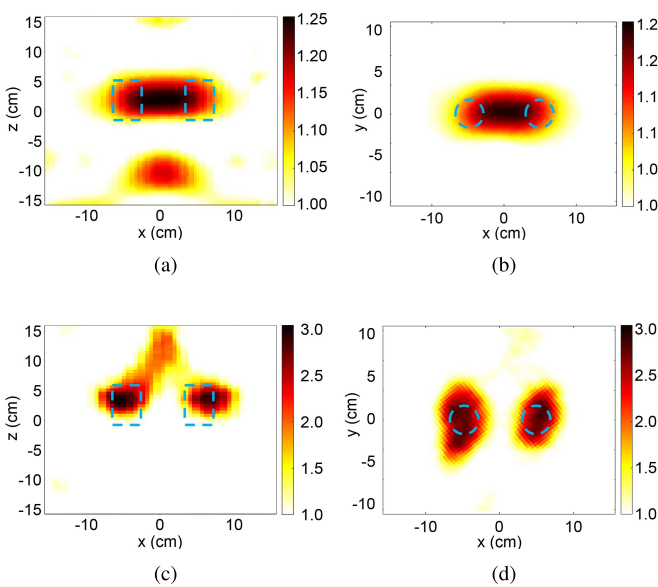


Fig. 20. Cross-sectional planes of the real part of the reconstructed dielectric map of the two nylon cylinders using “reconfigurable monopoles” at (a), (b) 1.47 and (c), (d) 1.75 GHz. Dashed lines: true position of the targets.

The reconfigurable-antenna system, shown in Fig. 19, was used to collect data for the same two nylon cylinders previously described and shown in Fig. 12. The FEM-CSI algorithm was again utilized to invert the collected data. Imaging results for two nylon cylinders at different frequencies are shown in Fig. 20.

It can be observed that the artifacts are reduced in the reconstructed image and the permittivity of the nylon cylinder is found to be closer to its actual value. Moreover, in the images of Fig. 20, the separation between the two cylinders is clearly visible and they are reconstructed closer to their true positions.

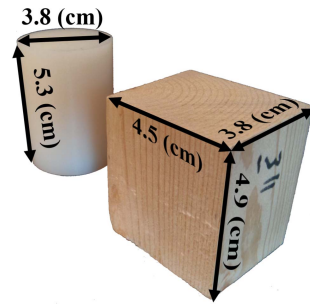


Fig. 21. Wooden cube and nylon cylinder used to evaluate the performance of the imaging system.

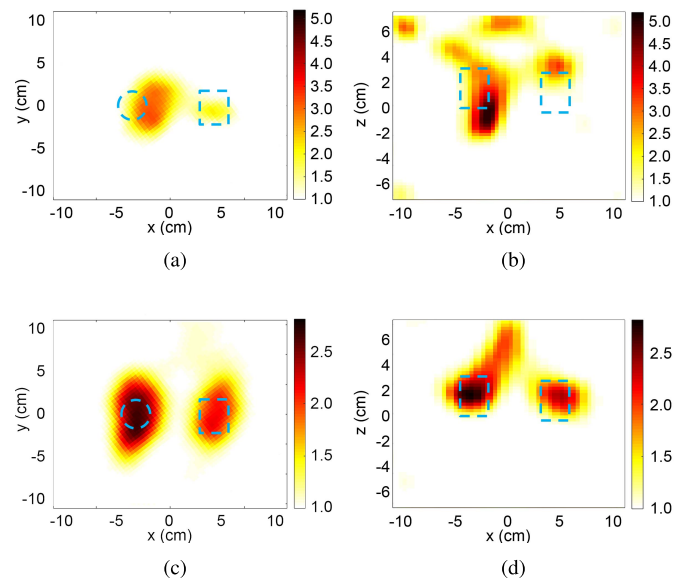


Fig. 22. Cross-sectional planes of the real part of the reconstructed dielectric map of the wooden cube and nylon cylinder using (a), (b) thin-wire monopoles and (c), (d) reconfigurable monopoles. Dashed lines: true position of the targets.

Furthermore, the permittivity of the reconstructed image is closer to its actual value. The percentage errors for this case are 44.05% and 7.20% for the 1.47- and 1.75-GHz reconstruction results. This improvement is due to the reduction in modeling error while maintaining a relatively high SNR as compared with the $\lambda/12$ antennas.

In order to further illustrate the effectiveness of using reconfigurable monopoles instead of the thin-wire monopole antennas, two targets of different dielectric permittivities were imaged using both systems. A picture of the targets used in this experiment is shown in Fig. 21. Note that the permittivity of the wooden cube is approximately 2.4. The reconstruction results for the data collected using these targets at 1.75 GHz are shown in Fig. 22. It can be observed that when the thin-wire monopoles are utilized, the reconstructed permittivity map is poor and includes many artifacts. However, the inversion results improve significantly when RAs are adopted. Not only the targets become discernible, their reconstructed permittivity gets very close to its true value as well. When the thin-wire monopoles and RAs are utilized for data acquisition, the percentage errors are 28.36% and 6.97%, respectively.

V. CONCLUSION

A novel 3-D MWI approach that uses metallic resonant chambers and, as data, utilizes measurements of the normal-field components at the surface of metallic chamber walls has been introduced. A detailed synthetic study was used to quantify the enhanced imaging performance that results from using such a configuration as compared with an unbounded domain system. Inversion results from an experimental system confirmed the enhanced performance, especially when RAs are utilized to collect the data. This paper explores one of the advantages of using metallic enclosures: being able to collect the normal-field component data right at the walls of the chamber. In the future work, we will investigate the advantages of utilizing the normal component in combination with the tangential magnetic field as data to improve imaging performance.

REFERENCES

- [1] W. C. Chew and Y. M. Wang, "Reconstruction of two-dimensional permittivity distribution using the distorted Born iterative method," *IEEE Trans. Med. Imag.*, vol. 9, no. 2, pp. 218–225, Jun. 1990.
- [2] A. Franchois and C. Pichot, "Microwave imaging-complex permittivity reconstruction with a Levenberg–Marquardt method," *IEEE Trans. Antennas Propag.*, vol. 45, no. 2, pp. 203–215, Feb. 1997.
- [3] J. De Zaeytijd, A. Franchois, C. Eyraud, and J.-M. Geffrin, "Full-wave three-dimensional microwave imaging with a regularized Gauss–Newton method—Theory and experiment," *IEEE Trans. Antennas Propag.*, vol. 55, no. 11, pp. 3279–3292, Nov. 2007.
- [4] A. Abubakar, P. M. van den Berg, and J. J. Mallorqui, "Imaging of biomedical data using a multiplicative regularized contrast source inversion method," *IEEE Trans. Microw. Theory Techn.*, vol. 50, no. 7, pp. 1761–1777, Jul. 2002.
- [5] A. Zakaria, C. Gilmore, and J. LoVetri, "Finite-element contrast source inversion method for microwave imaging," *Inverse Problems*, vol. 26, no. 11, p. 115010, Nov. 2010.
- [6] P. Mojabi and J. LoVetri, "Microwave biomedical imaging using the multiplicative regularized Gauss–Newton inversion," *IEEE Antennas Wireless Propag. Lett.*, vol. 8, pp. 645–648, 2009.
- [7] P. M. Meaney, M. W. Fanning, D. Li, S. P. Poplack, and K. D. Paulsen, "A clinical prototype for active microwave imaging of the breast," *IEEE Trans. Microw. Theory Techn.*, vol. 48, no. 11, pp. 1841–1853, Nov. 2000.
- [8] M. Asefi, M. Ostadrahimi, J. LoVetri, and L. Shafai, "Analysis of a 3D microwave imaging system," in *Proc. IEEE Antennas Propag. Soc. Int. Symp. (AP-S)*, Jul. 2013, pp. 608–609.
- [9] C. Gilmore, A. Zakaria, J. LoVetri, and S. Pistorius, "A study of matching fluid loss in a biomedical microwave tomography system," *Med. Phys.*, vol. 40, no. 2, p. 023101, Jan. 2013.
- [10] C. Gilmore, A. Zakaria, S. Pistorius, and J. LoVetri, "Microwave imaging of human forearms: Pilot study and image enhancement," *Int. J. Biomed. Imag.*, vol. 2013, no. 19, Jan. 2013, Art. no. 673027.
- [11] C. Yu *et al.*, "Active microwave imaging II: 3-D system prototype and image reconstruction from experimental data," *IEEE Trans. Microw. Theory Techn.*, vol. 56, no. 4, pp. 991–1000, Apr. 2008.
- [12] C. Gilmore and J. LoVetri, "Enhancement of microwave tomography through the use of electrically conducting enclosures," *Inverse Problems*, vol. 24, no. 3, p. 035008, Apr. 2008.
- [13] P. Mojabi, C. Gilmore, A. Zakaria, and J. LoVetri, "Biomedical microwave inversion in conducting cylinders of arbitrary shapes," in *Proc. 13th Int. Symp. Antenna Technol. Appl. Electromagn. Can. Radio Sci. Meeting*, Feb. 2009, pp. 1–4.
- [14] P. Mojabi and J. LoVetri, "Eigenfunction contrast source inversion for circular metallic enclosures," *Inverse Problems*, vol. 26, no. 2, p. 025010, Jan. 2010.
- [15] P. Mojabi and J. LoVetri, "A novel microwave tomography system using a rotatable conductive enclosure," *IEEE Trans. Antennas Propag.*, vol. 59, no. 5, pp. 1597–1605, May 2011.
- [16] M. Asefi, I. Jeffrey, J. LoVetri, C. Gilmore, P. Card, and J. Paliwal, "Grain bin monitoring via electromagnetic imaging," *Comput. Electron. Agricult.*, vol. 119, pp. 133–141, Nov. 2015.
- [17] A. Zakaria, M. Asefi, M. Ostadrahimi, I. Jeffrey, and J. LoVetri, "Electromagnetic imaging inside metallic enclosures using the normal boundary field components," in *Proc. USNC-URSI Radio Sci. Meeting*, Jul. 2014, p. 253.
- [18] M. Asefi, G. Faucher, and J. LoVetri, "Surface-current measurements as data for electromagnetic imaging within metallic enclosures," *IEEE Trans. Microw. Theory Techn.*, vol. 64, no. 11, pp. 4039–4047, Nov. 2016.
- [19] O. M. Bucci and T. Isernia, "Electromagnetic inverse scattering: Retrievable information and measurement strategies," *Radio Sci.*, vol. 32, no. 6, pp. 2123–2137, Nov./Dec. 1997.
- [20] O. M. Bucci, L. Crocco, and R. Scapaticci, "On the optimal measurement configuration for magnetic nanoparticles-enhanced breast cancer microwave imaging," *IEEE Trans. Biomed. Eng.*, vol. 62, no. 2, pp. 407–414, Feb. 2015.
- [21] M. Pastorino, *Microwave Imaging*, vol. 208. Hoboken, NJ, USA: Wiley, 2010.
- [22] P. M. van den Berg and R. E. Kleinman, "A contrast source inversion method," *Inverse Problems*, vol. 13, no. 6, p. 1607, 1997.
- [23] A. Zakaria, I. Jeffrey, and J. LoVetri, "Full-vectorial parallel finite-element contrast source inversion method," *Prog. Electromagn. Res.*, vol. 142, pp. 463–483, Sep. 2013.
- [24] R. J. Spiegel, C. A. Booth, and E. L. Branaugh, "A radiation measuring system with potential automotive under-hood application," *IEEE Trans. Electromagn. Compat.*, vol. EMC-25, no. 2, pp. 61–69, May 1983.
- [25] M. Ostadrahimi *et al.*, "Analysis of incident field modeling and incident/scattered field calibration techniques in microwave tomography," *IEEE Antennas Wireless Propag. Lett.*, vol. 10, pp. 900–903, Sep. 2011.
- [26] C. Gilmore *et al.*, "A wideband microwave tomography system with a novel frequency selection procedure," *IEEE Trans. Biomed. Eng.*, vol. 57, no. 4, pp. 894–904, Apr. 2010.
- [27] M. Ostadrahimi, A. Zakaria, J. LoVetri, and L. Shafai, "A near-field dual polarized (TE–TM) microwave imaging system," *IEEE Trans. Microw. Theory Techn.*, vol. 61, no. 3, pp. 1376–1384, Mar. 2013.

Mohammad Asefi (GS'16), photograph and biography not available at the time of publication.

Amer Zakaria (M'12), photograph and biography not available at the time of publication.

Joe LoVetri (SM'09), photograph and biography not available at the time of publication.